

# Optical control and coherent coupling of spin diffusive modes in thermal gases

P. Bevington<sup>1,\*</sup>, J. Nicholson<sup>2,\*</sup>, J. D. Zipfel<sup>1</sup>, W. Chalupczak<sup>1</sup>, C. Mishra<sup>2</sup>, and V. Guarrera<sup>2,†</sup>

<sup>1</sup>National Physical Laboratory, Hampton Road, Teddington, TW11 0LW, United Kingdom

<sup>2</sup>School of Physics and Astronomy, University of Birmingham, Edgbaston, Birmingham B15 2TT, United Kingdom



(Received 31 August 2023; accepted 26 March 2024; published 6 May 2024)

Quantum science and technology devices exploiting collective spins in thermal gases are extremely appealing due to their simplicity and robustness. This comes at the cost of dealing with the random thermal motion of the atoms which is usually an uncontrolled source of decoherence and noise. There are however conditions, for example, when diffusing in a buffer gas, where thermal atoms can occupy a discrete set of stable spatial modes. Diffusive modes can be extended or localized, have different magnetic properties depending on boundary conditions, and can react differently to external perturbations. Here, we selectively excite, manipulate, and interrogate the longest-lived of these modes by using laser light. In particular, we identify the conditions for the generation of modes that are exceptionally resilient to detrimental effects such as light induced frequency shifts and power-broadening, which are often the dominant sources of systematic errors in atomic magnetometers and comagnetometers. Moreover, we show that the presence of spatial inhomogeneities in the pump introduces a coupling that leads to a coherent exchange of excitation between the two longest-lived modes. Our results demonstrate that systematic engineering of the multi-mode nature of diffusive gases has great potential for improving the performance of quantum sensors based on alkali-metal thermal vapors, and opens new perspectives for quantum information applications.

DOI: [10.1103/PhysRevResearch.6.023134](https://doi.org/10.1103/PhysRevResearch.6.023134)

## I. INTRODUCTION

Due to their long-lived collective spin states, gaseous mixtures of alkali-metal and noble-gas atoms are widely applied in quantum optics and sensing. At room temperature, atoms in a low-pressure gas enclosed in a glass cell move along ballistic trajectories at velocities on the order of 100 m/s. Alkali-metal spin ensembles in these regimes rapidly reach the cell walls, where they get depolarized. To reduce this effect and increase the alkali-metal spins' polarization lifetime, it is common practice to fill the cell with  $10^{-1}$  to  $10^4$  Torr of a buffer gas, i.e., an inert or diatomic gas with low polarizability. Velocity-changing collisions with the buffer gas modify the thermal motion of the spins, which becomes diffusive. In these conditions, atoms can occupy different stable spatial modes. Few experiments have reported diffusion effects in the context of light storage and slowing-down [1,2], and atomic (nonspin) coherence [3]. The impact of diffusive spin dynamics has been recently considered for reducing noise and instability in ultrasensitive atomic sensors [4], for the realization and study of non-Hermitian systems [5], for the development of new quantum information protocols [6], and for the generation of nonlocal classical and nonclassical correlations [7,8]. Even though some signatures of different diffusive modes have been

detected in optically pumped atomic magnetometers [9,10], the effect of higher order modes on the collective spin dynamics has not been systematically analysed.

In the present paper, we directly access and characterize the underlying multi-mode dynamics of an atomic system in a range of parameters which is common for atomic magnetometry and comagnetometry. By using spatially resolved nondestructive spin imaging [11,12], we can identify the longest-lived stable modes with distinctive magnetic properties that correspond to low-order diffusive modes of the alkali-metal ensemble. Our measurements show that, since pump and probe interact differently with different modes, the collective spin dynamics develops features that crucially depend on the parameters of the light beams, such as intensity and shape. In analogy with the Ramsey-narrowing effect seen in EIT systems [3], we can create long-lived collective spin states for which the sensitivity to light shifts and power broadening is reduced by up to one order of magnitude with respect to spatially homogeneous optical pumping conditions. We also show that spatial modes with different magnetic properties can coherently exchange collective excitation. Interestingly, in the presence of a noble-gas buffer, a spatially inhomogeneous optical pumping can turn the coupling between different alkali-metal spatial modes from incoherent to coherent. This is remarkable, especially when considering that the mechanism underlying the coupling is based on random diffusive dynamics.

## II. STABLE SPATIAL MODES IN THERMAL VAPORS

We analyze the Faraday-type polarization rotation signal generated by the transverse spin excitation of an alkali-metal

\*These authors contributed equally to this work.

†v.guarrera@bham.ac.uk

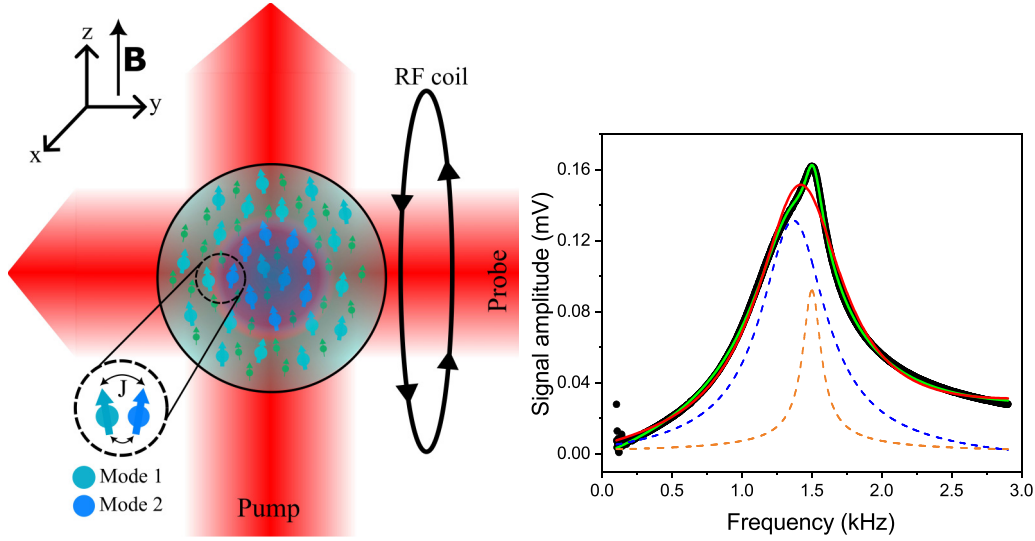


FIG. 1. Schematics of the experiment for excitation and probe of the alkali-metal and noble gas mixture. The spatially integrated spin-rotation signal is measured by a lock-in amplifier referenced to a RF modulation (see also Appendix A). The magnetic resonance shows a composite line shape: a bimodal Lorentzian function (solid green line) provides a significantly better fit to the data than a single Lorentzian function (solid red line), even in the presence of a nonuniform background to account for the offset at the tails of the signal. The dashed lines indicate the separate components of the bimodal Lorentzian fit.

gas in a spherical glass cell of 20 mm diameter, and containing 500 Torr of neon buffer gas (additional experimental details are available in Appendix A). The alkali spins are polarized along the axial magnetic field by a pump beam ( $\sigma$ -polarized, resonant with the  $F = 3 \rightarrow F' = 2$  transition for cesium, and roughly 10 mm diameter), and transverse excitation is generated by a weak RF resonant field; see Fig. 1. The neon gas is partially polarized by spin-exchange collisions with the polarized alkali atoms, and has an axial coherence time longer than 30 min. The cell also contains 30 Torr of nitrogen gas for quenching of the alkali excited states. The dynamics of the alkali transverse excitation is monitored for roughly 1 s after switching on the pump and the RF modulation. The signal is obtained by analyzing the polarization of a probe beam (linearly polarized and  $>15$  GHz detuned from any  $F = 4$  transition, and roughly 20 mm diameter), and is processed by a lock-in amplifier. We can perform both integrated and spatially resolved measurements. The latter are taken by shifting a mm-sized slit over the probe beam profile, which allows a mm-resolution to be obtained in the central region of the cell.

A careful inspection of the magnetic resonance line shape shows that it does not correspond to the single Lorentzian profile, which is typically associated with the lowest-order diffusion mode [3,10]; see Fig. 1. We interpret the observed additional features as different stationary spatial modes of the spins, which we identify as higher-order diffusion modes of the alkali-metal atoms. The diffusive dynamics of the spin excitation, in terms of the transverse magnetization  $S_+ = S_x + iS_y \equiv S$ , is described by the equation

$$\frac{\partial S}{\partial t} = D\nabla^2 S + \Gamma S, \quad (1)$$

where  $\Gamma = Dk^2$  is the relaxation rate due to collisions with the cell walls and diffusion effects,  $D$  is the diffusion coefficient, and  $k$  the wave-vector of the diffusive mode. Sta-

tionary spatial modes,  $s_{nl}(\mathbf{r})$ , can be obtained by solving the above Helmholtz equation with the Robin boundary condition [7,13,14]. For a spherical cell geometry, these solutions are in the form  $s_{nl}(\mathbf{r}) = j_l(k_{nl}r)Y_{lp}(\theta, \phi)$ , with  $j_l(x)$  the spherical Bessel functions of the first kind and  $Y_{lp}(\theta, \phi)$  the spherical harmonics. When the timescale of the diffusive dynamics is not larger than other spin decoherence effects, the evolution of  $S$  can then be expanded using the above modes with initial amplitude  $c_{nl}$ , obtained by convolution with the spatial profile of the pump beam or other pumping mechanisms. For simplicity of notation we reduce the index  $(n, l, p) = m$ , and we obtain

$$S = \sum_m c_m s_m(\mathbf{r}) e^{-(\Gamma_m + i\omega_m)t}, \quad (2)$$

where  $\omega_m$  is the precession frequency in the presence of a magnetic field,  $\Gamma_m = Dk_m^2 + \Gamma_d$ , and the decoherence rate  $\Gamma_d$  takes into account the spin destruction relaxations, spin exchange relaxations (alkali-alkali, alkali-noble gas), power broadening from the pump, and magnetic gradients [15,16].

Recorded spectra are fitted with a sum of  $\tilde{n}$  Lorentzian functions (see Appendix B), which leads to a very good agreement with  $\tilde{n} = 2$ , as shown in Fig. 1. This allows the main modes' parameters to be extracted, such as: the signal amplitude, decay rate, magnetic resonance frequency, and phase. The spatially resolved measurements, Fig. 2(a), show the existence of three main modes with different  $\Gamma_m$ , and allow their spatial distribution to be retrieved along the  $z$  axis (and integrated along the other two axis). A comparison with the lowest order symmetric diffusive modes provides a good quantitative agreement, once a Gaussian-shaped envelope for the probe beam is taken into account, Figs. 2(a) and 2(b). In particular, the measured ratios  $k_2/k_1 = 2.1(1)$  and  $k_3/k_1 = 3.1(2)$  are compatible with the theoretical predictions of  $k_2/k_1 = 2$  and  $k_3/k_1 = 3$ , in the regime of  $Dk_m^2 \gg \Gamma_d$  shown in Fig. 2(a). For the characterization of the regime  $Dk_m^2 \sim \Gamma_d$ , which is

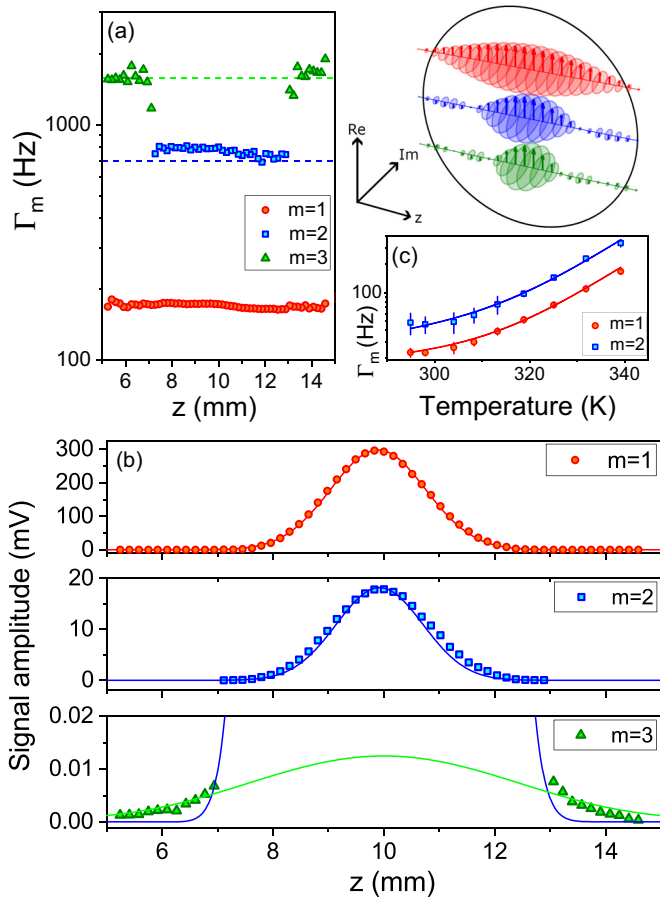


FIG. 2. (a) Linewidths of the two main Lorentzian components of the spatially resolved spin-rotation signal, along the  $z$  axis. Measurements are compared to the symmetric low-order diffusive modes of the atomic cell with largest coupling to the transverse Gaussian profile of the pump (shown in the cartoon inset  $s_{000}, s_{100}, s_{200}$ ). Dashed horizontal lines show the values of  $k_{100}/k_{000} = 2$  and  $k_{200}/k_{000} = 3$ . (b) Signal amplitude of each fitted mode as a function of the probe position along the  $z$  axis. Solid lines are fits obtained by convolution of the spatially integrated diffusive modes ( $s_{000}$  in red,  $s_{100}$  in blue,  $s_{200}$  in green) with the profile of the probe beam. (c) Temperature dependence of the  $m = 1, 2$  modes signal linewidth in a regime of  $Dk_m^2 \sim \Gamma_d$ . Solid lines are fits based on the temperature dependent model discussed in the text. Each data point is an average over at least 20 acquisitions.

of interest for precision (co)magnetometry, we have extracted information on the diffusive properties of the modes' by measuring their linewidth as a function of the sample temperature in the limit of low pump intensities (power  $\lesssim 30 \mu\text{W}$ ), to neglect the effects of power broadening, and for weak RF signal. The ratio between the linewidths of the first two modes does not change noticeably with temperature, which, for our system, is possible if the effective boundary conditions of the cell are temperature dependent, e.g., due to long range interaction with the atoms deposited at the cell walls [17]. Fitting with a model which takes account of this effect is shown in Fig. 2(c). Using the collisional cross sections and diffusion coefficients available in literature [18], we could retrieve from the fit a ratio  $k_2/k_1 = 1.9(1)$ , again compatible with predictions.

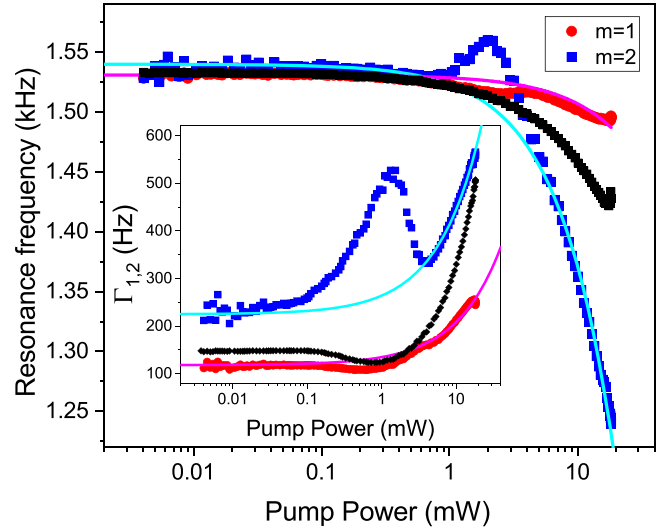


FIG. 3. Resonance frequency and linewidth of the modes  $m = 1, 2$  as a function of the pump power. Solid lines are fits to the asymptotic behavior, showing the light-induced shift and broadening of the two magnetic resonances. The features visible around 2 mW will be discussed later in the text. Black diamonds correspond to a single Lorentzian fit of the same data (i.e., no spatial-mode filtering applied). Each data point is a result of a fit over 100 acquisitions.

As alkali-metal gases are routinely interfaced with laser beams for manipulation and readout, it is important to test the behavior of the spatial modes in the dependence of such a perturbation assuming, at first, this is homogeneous along the beam's propagation direction. Fitting of the power broadening (in the limit of low temperatures  $T \leq 30^\circ\text{C}$ ), and of the light-induced Zeeman shift of the magnetic resonances [19] provides an average mutual scaling factor of 7.8(4) and 8.4(3) between the two main modes' (labeled  $m = 1, 2$ ) functional dependence on the pump beam intensity (see Fig. 3). Notably, the fundamental mode  $m = 1$  is not only the longest-lived diffusive mode, but it is also the mode whose main features (resonant frequency and linewidth) have a smoother dependence on pump intensity, without loss of signal amplitude. This effect can be explained as the atoms can move in and out of the pump beam, which has a Gaussian-like profile with a radius smaller than the radius of the cell [3,20]. In fact, we have verified that increasing the size of the pump beam can suppress shielding from the light-induced perturbation (see Appendix C), and it can change which of the available modes becomes dominant (for the same beam intensity). This will be particularly useful for performing differential measurements with the two longest-lived modes as they can be simultaneously optimized, differently for example from the case of Ref. [21]. Moreover, depending on the experimental conditions (i.e., pump size, shape, intensity) these preliminary measurements indicate that spatial-mode filtering of the signal can improve sensitivity of a magnetometer by a factor ranging between 1.15–5, and stability by, at least, a factor of 2 (evaluated at the maximum signal-to-noise ratio). This suggests that for the optimization of magnetometers and comagnetometers, the laser beams' parameters should be carefully calibrated with respect to the extension and features of the diffusive

modes supported by the cell geometry and conditions, and that spatial filtering is always beneficial [22].

### III. COUPLING OF SPATIAL MODES

Coherent and periodic exchange of spin excitation between an alkali-metal vapor and a noble gas has been recently demonstrated in the strong coupling regime [6]. The different intra-species modes can be projected onto a basis of diffusive spatial modes, which contribute independently to the overall transverse spin dynamics [8]. Moreover, studies of spatial modes' behavior in the context of parity-time (PT) symmetry breaking have been very recently conducted in a system of nuclear spins, with improved magnetometry demonstrated in the PT-broken phase [21].

Different stable spatial modes of a single atomic species do not usually coherently couple [8]. However, in the presence of a spatial inhomogeneity, such as a magnetic field gradient or a light-field gradient, a certain mixing of the different spatial modes might happen. In the simplifying assumptions of the spatial gradient adding to the Hamiltonian  $H_0 = D\nabla^2 - i\gamma B - \Gamma = D\nabla^2 - i\omega - \Gamma$  as a linear perturbation  $H_{\text{inh}} = -i\gamma Gz$  ( $G$  generally being a complex number), and in the approximation of considering the two longest-lived spatial modes: solutions of Eq. (1) can be sought in the form  $S(\mathbf{r}, t) = c_1(t)s_1(\mathbf{r}) + c_2(t)s_2(\mathbf{r})$ , where  $s_1(\mathbf{r}) = s_{000}(r, \theta, \phi)$ , and  $s_2(\mathbf{r}) = s_{011}(r, \theta, \phi)$ . In this case, the coefficients  $c_1, c_2$  evolve according to the equations (see also Ref. [21])

$$\begin{bmatrix} \dot{c}_1(t) \\ \dot{c}_2(t) \end{bmatrix} = \left( E_0 + \Delta \begin{bmatrix} 1 & J_1/\Delta \\ J_2/\Delta & -1 \end{bmatrix} \right) \begin{bmatrix} c_1(t) \\ c_2(t) \end{bmatrix}, \quad (3)$$

with  $E_0 = \frac{i(\omega_1 - \Gamma_1 + i\omega_2 - \Gamma_2)}{2}$ ,  $\Delta = \frac{i(\omega_1 - \Gamma_1 - i\omega_2 + \Gamma_2)}{2}$ , and  $J_{1,2} = -i\gamma G \int s_{1,2}^*(\mathbf{r}) z s_{2,1}(\mathbf{r}) d\mathbf{r}$  the coupling between the spatial modes due to the inhomogeneity, whose amplitude can be contracted as  $|J| = \sqrt{|J_1||J_2|}$ . In the limit of  $|J/\Delta| > 1$ , the spatial modes of the transverse collective spins can become coherently coupled. In our case where  $\omega_1 \sim \omega_2$  and  $\Gamma_1 \sim \Gamma_2/2$ ,  $|J| > \Delta \sim \Gamma_1/2$  and the effects of the coupling might become visible as an exchange of collective spin excitations between the two spatial modes [23].

We analyze the transverse spin excitation induced by the weak RF field, for a fixed interrogation time, when varying the pump beam intensity. At a position  $z$  in the cell the features of the magnetic resonances are mainly determined by optical pumping and spin-exchange processes. Thus, in an optically thick cloud, the competition between these mechanisms can result in a spatial variation of the resonance frequency (and generally, of all the magnetic properties), and a gradient-induced coupling  $J$  between the spatial modes might appear. For low pump powers, when the beam intensity rapidly decays as it propagates inside the cell, the atoms mainly evolve in the dark. Spin-exchange collisions (including polarizing collisions with the noble gas) and diffusive dynamics dominate. The magnetic properties along the  $z$  direction are rather uniform and the spatial modes appear symmetric; see Fig. 4(a). By increasing the pump power, as the beam penetrates more deeply inside the cell, the competition between regions of the cell dominated by optical pumping or by spin-exchange interaction leads to a larger inhomogeneity in the magnetic

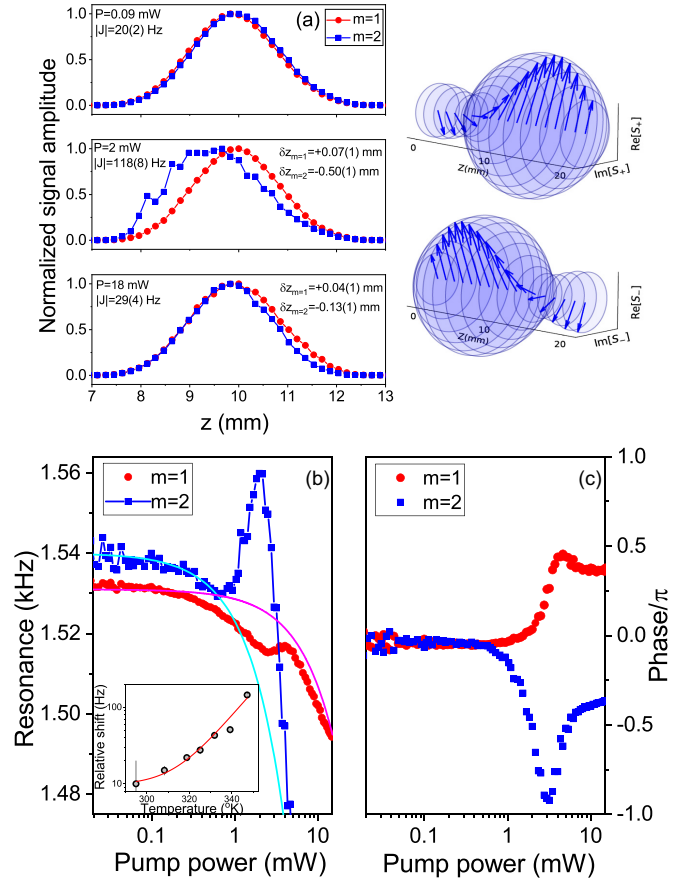


FIG. 4. (a) Spatial imaging of the two main spin modes along the pump direction, recorded for different pump powers. Fitted displacement of the modes from their initial position is shown, together with  $|J|$  obtained from the same spin imaging measurements (see also Appendix A). Plots of the inhomogeneous case eigenmodes  $s_{\pm}(\mathbf{r})$  are shown on the side. (b, c) Zooms of the pump power dependence of the resonance frequency and phase show the two modes shifting in opposite directions, before the signal is dominated by the light-induced shifts (shown with solid lines). In the inset: peak resonance frequency separation between the modes  $m = 1, 2$  for intermediate pump powers as a function of temperature. Red solid line is a fit showing a linear dependence on the atomic density.

properties of the alkali gas, such that  $|J/\Delta|$  becomes larger than 1. In this case, we observe that the two main spin modes separate spatially as in Fig. 4(a), resembling the  $s_{\pm}(\mathbf{r}) = s_1(\mathbf{r}) \pm s_2(\mathbf{r})$  modes. In parallel, as  $|J/\Delta|$  increases [e.g., from 0.23(3) at 0.09 mW pump power, to 1.2(1) at 2 mW for the data in Figs. 4(b) and 4(c)], both the resonance frequencies and the phases of these modes shift apart as expected in the presence of coupling. Analysing this region of parameters, we find that, the frequency shift between the two modes shows dependence on the alkali-metal atomic density, see inset of Fig. 4(b). This is related to: the change of on-resonance optical thickness ( $2N_A\sigma_{32}R$ , where  $N_A$  is the atomic density,  $\sigma_{32}$  the on-resonance scattering cross-section for the pumping transition, and  $R$  the radius of the cloud), and to the magnetic frequency shift induced by the magnetization of the noble-gas ( $M \propto k_{SE}N_A p_A$ , where  $p_A$  is the polarization of the alkali-metal atoms). Finally, further increase of the pump power



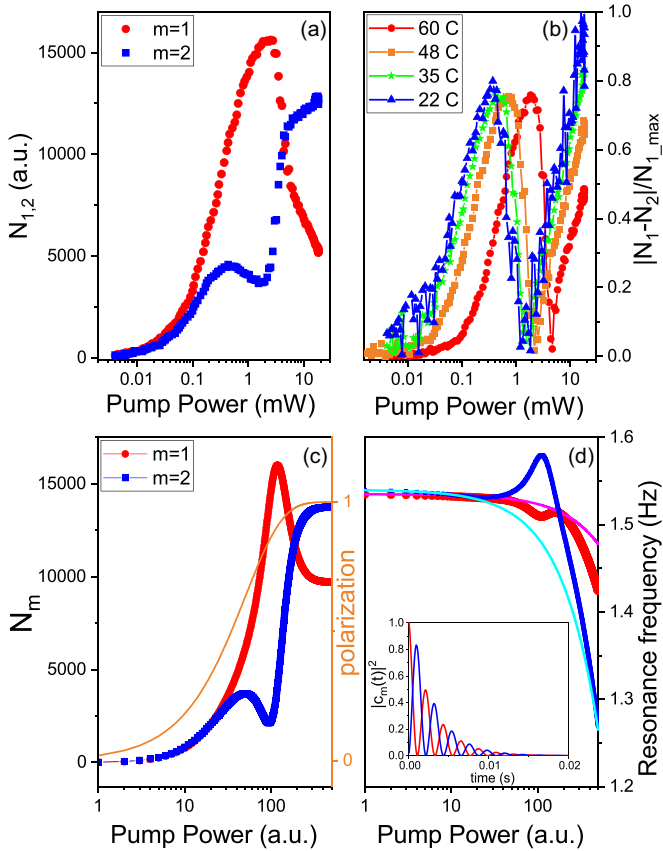


FIG. 5. (a) Number of excitations  $N_{1,2}$  for the two main spatial modes as a function of the pump power. (b) The normalized difference of excitations as a function of the pump power, measured for different temperatures. (c) Results obtained with a simple model based on Eqs. (3). The experimentally derived parameters were used, and  $|J_1|$  was set in the range  $(0.5-0.9)|J_2|$ , and  $|J| = \sqrt{|J_1||J_2|} = 8\Gamma_1$ . The solid line shows the degree of optically induced alkali-metal polarization. (d) The calculated resonance frequencies as a function of the pump power are displayed together with solid lines showing the experimentally derived asymptotic behavior. The inset shows the exchange of collective excitations between the two modes for a pump power of 100 (a.u.).

determines a progressively more homogeneous optical pumping along  $z$ , and the saturation of the atomic cloud, Fig. 4(a). In this regime of strong pump, the light-induced frequency shift and linewidth broadening also become significant. As a result,  $|J/\Delta|$  decreases [e.g., it becomes equal to 0.39(8) at 18 mW], the coupling ceases, and the two spatial modes appear to evolve independently again. To obtain further insight on the coupled dynamics, for each detected mode we have derived the total number of spin excitations by integrating the corresponding magnetic resonance on both the standard X and Y signals of the lock-in amplifier for a fixed interrogation time. An example of the resulting measurements is shown in Figs. 5(a) and 5(b). For lower pump powers [e.g.,  $\lesssim 0.1$  mW, in the same experimental conditions of Figs. 4(b) and 4(c)], the excitation of the two spatial modes shows a similar growth. For higher powers, the modes show an anticorrelated nonmonotonic evolution, which appears as an exchange of excitation down to roughly 7 mW pump power. The main

features of this behavior shift towards lower pump powers for decreasing temperatures, see Fig. 5, which can be explained with the change of the on-resonance optical thickness of the atomic cloud. In fact, the mode coupling appears when the cloud is only partially optically pumped, which corresponds to lower values of the pump power for a decreased optical thickness.

We have solved a simple model based on Eq. (3), with in addition  $|J| \propto (N_A p_A)$  and a term of gain, both taking into account the variation, and saturation, of the optical pumping, see Appendix B for further details. The agreement with the measurements is qualitatively good, as shown in Fig. 5. The model confirms that the details of the excitation, such as the appearance of the anticorrelated signals, derive from the coupling between the modes and depend on the optical saturation of the cloud. The model also allows us to calculate the time-dependent dynamics of the excitation [24], which shows a coherent exchange between the two spatial modes for the region of parameters where the anticorrelated signal is visible [inset of Fig. 5(d)]. Note that initially,  $S(\mathbf{r}, t \simeq 0) \simeq s_1(\mathbf{r})$ , due to  $J_1 < J_2$  and  $\Gamma_1 < \Gamma_2$ . From a quantitative point of view, the model best fits the data with a coupling coefficient  $|J| \sim 8\Gamma_1$ . This is roughly a factor of 7 larger than the measured values of  $|J|$ , which are however just rough estimates of the inhomogeneity (see Appendix A). Finally, we have repeated the measurements with a miniature cell containing cesium and roughly 200 Torr of nitrogen. The amount of excitation for the main two modes as a function of the pump power does not appear to be anticorrelated, which we have quantified by calculating the Spearman correlation coefficient between the two modes (which is  $-0.37$  for the system with neon, and  $+0.9$  for the system without neon at temperatures between 80 and 100 °C, see the Appendix D). Also, no opposite shifts of the magnetic resonances have been detected. Note that, neon's magnetization contributes to  $G$ , as spin-exchange collisions between alkali and noble gas shift the precession frequency of the former with opposite sign with respect to the light shift (see also Appendix A). In addition, in the miniature cell with pure nitrogen buffer, the difference in linewidth between the modes is increased with respect to the spherical cell, due to different boundary conditions. As a result  $|J/\Delta| \ll 1$ , and the coupling between the modes is expected to be negligible.

#### IV. CONCLUSIONS

Our work demonstrates that multi-mode filtering and manipulation of the collective spin dynamics are powerful tools to enhance the performances of quantum devices for sensing, and it should be especially considered in the context of precision comagnetometry measurements [25], and in schemes involving self-organizing mechanisms, e.g., the spin maser [26]. Independent spatial control obtained by the combined use of laser light and magnetic fields, which is only possible in alkali-metal gases, can lead to engineering the dissipative coupling between diffusive modes, and to further coherence preservation [5]. Moreover, future developments include the study of optically driven, localized magnetic structures [27], also in the context of the study of phase transitions [28], and the interaction with complex twisted light [29]. Finally, the coherent coupling of localized alkali-metal modes opens

exciting perspectives for quantum imaging and storage of optical information [30].

### ACKNOWLEDGMENTS

The work was supported by the EPSRC (Grants No. EP/S000992/1 and No. EP/Y004817/1) and by the UK Department for Science, Innovation and Technology (DSIT). We thank R. Hendricks and G. Barontini for critical reading of manuscript. We acknowledge useful discussions with Curt von Keyserlingk.

### APPENDIX A: EXPERIMENTAL SETUP AND ESTIMATE OF THE SPATIAL INHOMOGENEITY

The measurements described here are performed in a shielded setup, with the atomic vapor cell enclosed in a 3D-printed oven driven by an AC current modulated at a frequency of 100 KHz. Because of the cell spherical shape, three sets of heaters are used to heat the cell. Pumping is performed by one or a pair of circularly polarised laser beams, frequency stabilized to the  $6^2S_{1/2} F = 3 \rightarrow 6^2P_{3/2} F' = 2$  transition (D2 line, 852 nm), propagating along the direction of the bias static magnetic field, Fig. 1 in the main text. The power of the pump beam is controlled by an acousto-optic modulator (AOM) operating in the double passage configuration. The pump beam's size is adjusted by a beam expander. The ambient magnetic field is suppressed by the use of five layers of cylindrical shields made from 2 mm thick mu-metal with end caps (suppression factor of  $10^6$ ). A pair of solenoids inside the shield generates a well-controlled bias magnetic field, with a relative homogeneity at the level of  $10^{-4}$  over the length of the cell. A set of Helmholtz coils orthogonal to the axis of the bias magnetic field produces the weak RF magnetic field that drives the atomic coherence. Paramagnetic Faraday rotation maps the value of the collective atomic spin onto the polarization state of the linearly polarised probe beam [31–33] that propagates orthogonally to the pump beams. After the atomic cell, the probe beam passes through a polarization analyser, and two orthogonal polarization components are measured by a balanced photodetector. The resulting signal is then measured by a lock-in amplifier referenced to the first harmonic of the RF field frequency.

Spatially resolved spin imaging allows us to derive an estimate of the inhomogeneous conditions through the sample ( $G$ ). As this estimate is different for the two modes we calculate the total coupling as  $|J| = \sqrt{|J_1||J_2|}$ . In the estimate of  $|J|$ , we account both for the inhomogeneity in the frequency (imaginary part) and in the linewidth of the two modes' magnetic signal (real part). The accuracy of this estimate is limited by the thermal motion of the atoms [ $\Re(G)$  and  $\Im(G)$  are correlated], and overlap with the pump beam in the transverse direction (here not seen). Example measurements are shown in Fig. 6.

### APPENDIX B: FITTING AND NUMERICAL MODEL

Magnetic resonances, like those detected in the present paper, can be fitted with a curve which has a component with an absorptive character that is in-phase with the

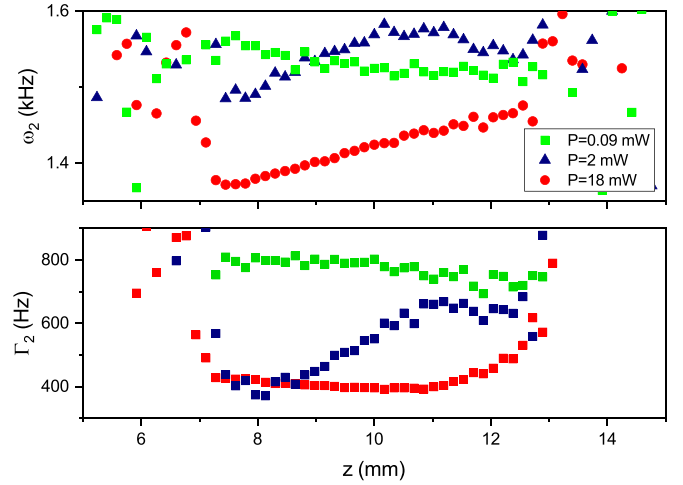


FIG. 6. Spin imaging showing spatial dependence of the precession frequency (above), and linewidth (below) of the magnetic resonance of mode  $m = 2$ . This mode, being spatially localized, more evidently shows dependence on local conditions.

oscillating RF-field (usually referred to as  $X$ ), and a component with a dispersive character that is  $90^\circ$  out-of-phase with the oscillating RF-field ( $Y$ ). More explicitly,

$$X(\nu) = \frac{\Gamma/(2\pi)}{(\nu - \nu_0)^2 + (\Gamma/2)^2},$$

$$Y(\nu) = \frac{(\nu - \nu_0)/\pi}{(\nu - \nu_0)^2 + (\Gamma/2)^2},$$

where  $\Gamma$  and  $\nu_0$  are, respectively, the FWHM and central frequency of the magnetic resonance. The amplitude of the magnetometer response  $R$  can thus be obtained as the amplitude of a complex Lorentzian lineshape, with  $X$  and  $Y$  being its real and imaginary components. Here, we have fitted both the  $X$  and  $Y$  signals provided by a lock-in amplifier referenced to the RF field frequency (and reconstructed  $R$ ), by allowing a possible phase shift  $\theta_j$  between signal and reference. For each mode  $j = 1, 2$ :

$$X_j(\nu) = \frac{A_j \Gamma_j}{(\nu - \nu_j)^2 + (\Gamma_j/2)^2} \cos(\theta_j) - 2 \frac{A_j(\nu - \nu_j)}{(\nu - \nu_j)^2 + (\Gamma_j/2)^2} \sin(\theta_j),$$

$$Y_j(\nu) = \frac{A_j \Gamma_j}{(\nu - \nu_j)^2 + (\Gamma_j/2)^2} \sin(\theta_j) + 2 \frac{A_j(\nu - \nu_j)}{(\nu - \nu_j)^2 + (\Gamma_j/2)^2} \cos(\theta_j),$$

with  $A_j$  the modes' amplitude. To take into account for the asymmetry in the tails of our experimental curves we have added an inhomogeneous linear background to the fitting function. We note that fitting the background with either a uniform, linear, or Lorentzian function does not have any relevant impact on the results obtained from the bimodal Lorentzian fitting. As an overall fit to the tails of our measurements, we note also that both a linear and a Lorentzian background provide a very good matching with the experimental data. This fact, together with the unambiguous detection of a third

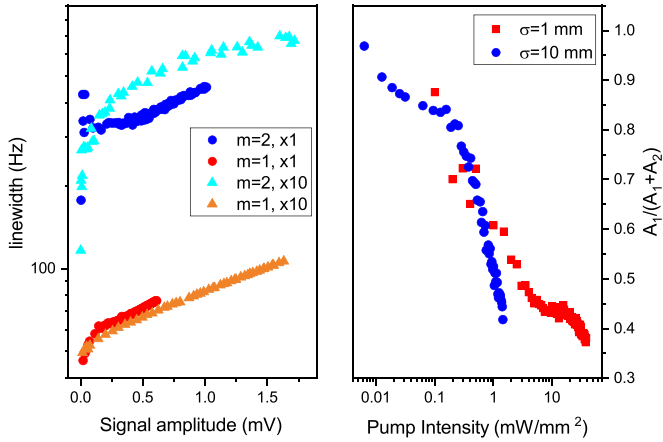


FIG. 7. On the left: linewidth dependence on signal amplitude for two different Gaussian beam sizes corresponding respectively to  $\sigma = 1$  mm ( $\times 1$ ), and  $\sigma = 10$  mm ( $\times 10$ ), measured before the atomic cell. On the right: the relative amplitude of the two main modes is affected by both intensity and size of the pump. Changing these parameters it would be possible to tune in a controlled way the contribution of each mode to the final detected signal.

diffusive mode in some experimental conditions [as those of Figs. 2(a) and 2(b) in the main text], suggests that the origin of the inhomogeneous background could be related to the presence of additional higher-order diffusive modes, with significantly shorter lifetime than the two main modes considered in the present paper.

To obtain the numerical values of  $N_j$  shown in Figs. 5(c) and 5(d) of the main text we have solved Eq. (3):

$$\begin{aligned}\dot{c}_1(t) &= i(\omega_1 - \omega_{L1}x)c_1(t) - \Gamma_1 c_1(t) + J_1 f(x)c_2(t) \\ &\quad + p_1 f(x), \\ \dot{c}_2(t) &= i(\omega_2 - \omega_{L2}x)c_2(t) - \Gamma_2 c_2(t) + J_2 f(x)c_1(t) \\ &\quad + p_2 f(x),\end{aligned}$$

where the frequencies  $\omega_j = 2\pi\nu_j$ , the light shifts  $\omega_{Lj}$ , the linewidths  $\Gamma_j$ , and the effective pump amplitudes  $p_j$  have been obtained from our experimental data, while the modes' couplings  $J_{1,2}$  have been left as free parameters. Note that  $x$  is an adimensional parameter representing the pump power, which we have used to account for the effects of light shifts and optical polarization of the cloud, as the function  $f(x) \propto (1 - e^{-x})$  approximates the dependence of the degree of optically induced-polarization on pump power  $x$  (see Fig. 5(c) in the main text). Finally,  $N_j$  have been calculated by integrating  $|c_j(t)|^2$  over our observation time (1 s).

#### APPENDIX C: CONTROL VIA ADJUSTMENT OF THE PUMP BEAM

We have characterized the magnetic signal for two different pump beam sizes, i.e.,  $\sigma = 1$ –10 mm, where the Gaussian beam profiles are measured in front of the atomic cell. In particular, we have observed a narrowing of the linewidth of the second-order mode  $m = 2$  by 150 Hz as a result of the beam narrowing, for the same signal amplitudes (data above 0.3 mV in Fig. 7). As we have verified using nonresonant

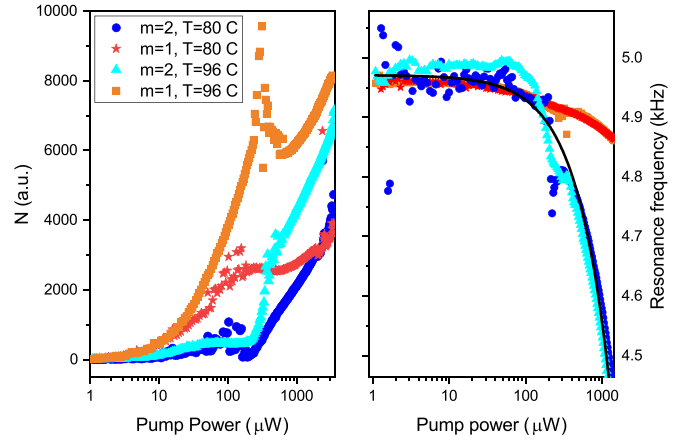


FIG. 8. Number of excitations (left) and resonance frequency (right) as a function of the pump power, measured for a wafer cell containing cesium and Nitrogen buffer (pressure roughly 200 Torr). Black solid line is a linear fit to the data.

light, the distortion of the beam introduced by the spherical glass cell prevents us from obtaining a clean Gaussian profile with size  $\sigma \gtrsim 6$  mm. As a result, the  $m = 2$  spatial mode can be either mostly or partially covered by the pump beam, while the more extended  $m = 1$  spatial mode is always unevenly or partially covered. Hence, the different behavior of the two modes, with the  $m = 1$  linewidth showing no clear dependence on the pump beam size in this range of parameters. We observe also that both intensity and size of the pump beam affect the relative amplitude of the spatial modes, and by modifying one of these parameter it would be possible to change which mode is dominantly contributing to overall signal, for equal detection; see Fig. 7. We foresee that a more sophisticated shaping of the pump beam profile, e.g., with the use of structured or chiral light, and a different realization of the cell could also contribute to control the excitation of different spatial modes within the atomic cell.

#### APPENDIX D: ATOMIC CELL WITHOUT NEON BUFFER

The measurements presented in the text have been repeated in a cell containing a solid sample of cesium and a buffer of roughly 200 Torr of Nitrogen alone. The cell is built on a silicon wafer substrate and is made of two connected glass chambers with the cesium sample being hosted in one of them (INEX Microtechnology). The chamber used for the measurements has a rectangular shape with size  $4 \times 4$  mm<sup>2</sup> and thickness of 2 mm. The heater is supplied by an AC current modulated at a frequency of 1 MHz.

Analogously to the measurements in the presence of the neon buffer, the magnetic resonance peaks show composite shapes, hence we can similarly derive information on the main stationary spatial modes of the alkali-metal atoms, see Fig. 8. To quantify the mutual dependence and the presence of any correlation (or anticorrelation) in the excitation of the two main modes as a function of the pump power, we have calculated their Spearman correlation coefficient ( $-1 \leq \rho \leq 1$ ). For the measurements with neon at 60 °C, the correlation

coefficient has a negative value  $\rho = -0.37$  signaling the presence of a partial anticorrelation (and  $\rho = -0.95$  for pump powers larger than 0.8 mW). In the case without neon, instead, the correlation parameter has a value  $\rho = +0.91$  signaling the presence of a strong positive correlation for the measurements at a temperature of 80 °C, and just slightly less  $\rho = +0.88$  for the measurements at 96 °C. At a temperature of 50–60 °C the precession frequency does not show any shift, apart from the expected light-induced one. Some features are visible for

temperatures above 80 °C, corresponding to a regime where the optical thickness of the atomic cloud falls in the range of the neon cell measurements. These are qualitative different than those observed in the neon buffer cell (for instance the frequency shift for the two modes has the same sign), and can be explained as a competition between optical pumping and intra-species spin exchange interactions. Their analysis is beyond the scope of the present work and it will be further discussed in a future publication.

- 
- [1] M. Shuker, O. Firstenberg, R. Pugatch, A. Ron, and N. Davidson, Storing images in warm atomic vapor, *Phys. Rev. Lett.* **100**, 223601 (2008).
  - [2] O. Firstenberg, P. London, D. Yankelev, R. Pugatch, M. Shuker, and N. Davidson, Self-similar modes of coherent diffusion, *Phys. Rev. Lett.* **105**, 183602 (2010).
  - [3] Y. Xiao, I. Novikova, D. F. Phillips, and R. L. Walsworth, Diffusion-induced Ramsey narrowing, *Phys. Rev. Lett.* **96**, 043601 (2006).
  - [4] W. Xiao, M. Liu, T. Wu, X. Peng, and H. Guo, Femtotesla atomic magnetometer employing diffusion optical pumping to search for exotic spin-dependent interactions, *Phys. Rev. Lett.* **130**, 143201 (2023).
  - [5] Y. Li, Y.-G. Peng, L. Han, M.-L. Miri, W. Li, M. Xiao, X.-H. Zhu, J. Zhao, A. Alu, S. Fan, and C.-W. Qiu, Antiparity-time symmetry in diffusive systems, *Science* **364**, 170 (2019).
  - [6] R. Shaham, O. Katz, and O. Firstenberg, Strong coupling of alkali-metal spins to noble-gas spins with an hour-long coherence time, *Nat. Phys.* **18**, 506 (2022).
  - [7] R. Shaham, O. Katz, and O. Firstenberg, Quantum dynamics of collective spin states in a thermal gas, *Phys. Rev. A* **102**, 012822 (2020).
  - [8] O. Katz, R. Shaham, and O. Firstenberg, Quantum interface for noble-gas spins based on spin-exchange collisions, *PRX Quantum* **3**, 010305 (2022).
  - [9] J. Skalla, G. Wackerle, M. Mehring, and A. Pines, Optical magnetic resonance imaging of Rb vapor in low magnetic fields, *Phys. Lett. A* **226**, 69 (1997).
  - [10] S. Knappe and H. G. Robinson, Double-resonance lineshapes in a cell with wall coating and buffer gas, *New J. Phys.* **12**, 065021 (2010).
  - [11] H.-F. Dong, J.-L. Chen *et al.*, Spin image of an atomic vapor cell with a resolution smaller than the diffusion crosstalk free distance, *J. Appl. Phys.* **125**, 243904 (2019).
  - [12] H. Xia, A. Ben-Amar Baranga, D. Hoffman, and M. Romalis, Magnetoencephalography with an atomic magnetometer, *Appl. Phys. Lett.* **89**, 211104 (2006).
  - [13] Z. Wu, S. Schaefer, G. D. Cates, and W. Happer, Coherent interactions of the polarized nuclear spins of gaseous atoms with the container walls, *Phys. Rev. A* **37**, 1161 (1988).
  - [14] F. Masnou-Seeuws and M. A. Bouchiat, Étude théorique de la relaxation d'atomes alcalins par collisions sur une paroi et sur un gaz, *J. Phys. France* **28**, 406 (1967).
  - [15] R. K. Ghosh and M. V. Romalis, Measurement of spin-exchange and relaxation parameters for polarizing  $^{21}\text{Ne}$  with K and Rb, *Phys. Rev. A* **81**, 043415 (2010).
  - [16] W. Happer and A. C. Tam, Effect of rapid spin exchange on the magnetic resonance spectrum of alkali vapors, *Phys. Rev. A* **16**, 1877 (1977).
  - [17] In support of this statement, we have seen that the resonance linewidth irreversibly broadens with increasing temperature of the cell, which means that, once broadened, it does not regain its initial value even after the heating system is switched off. This excess broadening disappears only after the cell is removed from the apparatus and the glass is cleaned from the residual alkali-metal adsorbed at its surface.
  - [18] J. W. Lou and G. A. Cranch, Characterization of atomic spin polarization lifetime of cesium vapor cells with neon buffer gas, *AIP Adv.* **8**, 025305 (2018).
  - [19] B. S. Mathur, H. Tang, and W. Happer, Light shifts in the alkali atoms, *Phys. Rev.* **171**, 11 (1968).
  - [20] D. Hunter, T. E. Dyer, and E. L. Riis, Accurate optically pumped magnetometer based on Ramsey-style interrogation, *Opt. Lett.* **47**, 1230 (2022).
  - [21] X. Zhang, J. Hu, and Zhao, Stable atomic magnetometer in parity-time symmetry broken phase, *Phys. Rev. Lett.* **130**, 023201 (2023).
  - [22] J. D. Zipfel, P. Bevington, L. Wright, W. Chalupczak, G. Quick, B. Steele, J. Nicholson, and V. Guarrera, Indirect pumping of alkali-metal gases in a miniature silicon-wafer cell, *arXiv:2402.16695*.
  - [23] Y.-L. Fang, J.-L. Zhao, Y. Zhang, D.-X. Chen, Q.-C. Wu, Y.-H. Zhou, C.-P. Yang, and F. Nori, Experimental demonstration of coherence flow in PT- and anti-PT-symmetric systems, *Commun. Phys.* **4**, 223 (2021).
  - [24] Measurement of the dynamics during the transient would alter the magnetic properties of the modes, e.g., the linewidth, and will thus impact the estimate of the total number of excitation for each mode.
  - [25] T. Sato *et al.*, Development of colocated  $^{129}\text{Xe}$  and  $^{131}\text{Xe}$  nuclear spin masers with external feedback scheme, *Phys. Lett. A* **382**, 588 (2018).
  - [26] W. Chalupczak and P. Josephs-Franks, Alkali-metal spin maser, *Phys. Rev. Lett.* **115**, 033004 (2015).
  - [27] B. Schäpers, M. Feldmann, T. Ackermann, and W. Lange, Interaction of localized structures in an optical pattern-forming system, *Phys. Rev. Lett.* **85**, 748 (2000).
  - [28] Y. Horowicz, O. Katz, O. Raz, and O. Firstenberg, Critical dynamics and phase transition of a strongly interacting warm spin gas, *Proc. Natl. Acad. Sci. USA* **118**, e2106400118 (2021).
  - [29] M. Babiker, D. L. Andrews, and D. E. Lembessis, Atoms in complex twisted light, *J. Opt.* **21**, 013001 (2019).



- [30] J. Sun, X. Zhang, W. Qu, E. E. Mikhailov, I. Novikova, H. Shen, and Y. Xiao, Spatial multiplexing of squeezed light by coherence diffusion, [Phys. Rev. Lett. \*\*123\*\*, 203604 \(2019\)](#).
- [31] Y. Takahashi, K. Honda, N. Tanaka, K. Toyoda, K. Ishikawa, and T. Yabuzaki, Quantum nondemolition measurement of spin via the paramagnetic Faraday rotation, [Phys. Rev. A \*\*60\*\*, 4974 \(1999\)](#).
- [32] I. M. Savukov, S. J. Seltzer, M. V. Romalis, and K. L. Sauer, Tunable atomic magnetometer for detection of radio-frequency magnetic fields, [Phys. Rev. Lett. \*\*95\*\*, 063004 \(2005\)](#).
- [33] W. Chalupczak, R. M. Godun, S. Pustelny, and W. Gawlik, Room temperature femtotesla radio-frequency atomic magnetometer, [Appl. Phys. Lett. \*\*100\*\*, 242401 \(2012\)](#).